# Structural and Dynamic Studies on Ligand-Free Adenylate Kinase from *Mycobacterium tuberculosis* Revealed a Closed Conformation that Can Be Related to the Reduced Catalytic Activity[†,‡]

Simona Miron,*[,‡,§] Hélène Munier-Lehmann,[||,⊥] and Constantin T. Craescu*[,§]

*Institut National de la Santé et de la Recherche Médicale U350 et Institut Curie-Recherche, Centre Universitaire, Bâtiments 110-112, F-91405 Orsay, France, and Laboratoire de Chimie Structurale des Macromolécules (CNRS, URA 218), Institut Pasteur, Paris, France*

*Received September 5, 2003; Revised Manuscript Received November 3, 2003*

ABSTRACT: Tuberculosis is the leading cause of death worldwide from a single infectious disease. Search of new therapeutic tools requires the discovery and biochemical characterization of new potential targets among the bacterial proteins essential for the survival and virulence. Among them are the nucleoside monophosphate kinases, involved in the nucleotide biosynthesis. In this work, we determined the solution structure of adenylate kinase (AK) from *Mycobacterium tuberculosis* (AKmt), a protein of 181 residues that was found to be essential for bacterial survival. The structure was calculated by a simulated annealing protocol and energy minimization using experimental restraints, collected by nuclear magnetic resonance spectroscopy. The final, well-defined 20 NMR structures show an average root-mean-square deviation of 0.77 Å for the backbone atoms in regular secondary structure segments. The protein has a central CORE domain, composed of a five-stranded parallel $\beta$-sheet surrounded by seven α-helices, and two peripheral domains, AMPbd and LID. As compared to other crystallographic structures of free form AKs, AKmt is more compact, with the $AMP_{bd}$ domain closer to the CORE of the protein. Analysis of the $^{15}N$ relaxation data enabled us to obtain the global rotational correlation time (9.19 ns) and the generalized order parameters ($S^2$) of amide vectors along the polypeptide sequence. The protein exhibits restricted movements on a picosecond to nanosecond time scale in the secondary structural regions with amplitudes characterized by an average $S^2$ value of 0.87. The loops $\beta$1/α1, $\beta$2/α2, α2/α3, α3/α4, α4/$\beta$3, $\beta$3/α5, α6/α7 (LID), α7/α8, and $\beta$5/α9 exhibit rapid fluctuations with enhanced amplitudes. These structural and dynamic features of AKmt may be related to its low catalytic activity that is 10-fold lower than in their eukaryote counterparts.

Adenylate kinases (AKs)[1] are ubiquitous small enzymes, which play a key role in the energetic metabolism and nucleic acid synthesis (*1*, *2*). They catalyze the reversible transfer of the terminal phosphate group between ATP:$Mg^{2+}$ and AMP. A sequence comparison of different AKs split them into two groups: short variants (with about 190 residues) and long variants (between 214 and 238 residues) having an additional domain, called LID. Generally, the eukaryote cytosolic enzymes are short variants, whereas the bacterial, yeast, and mitochondrial AKs are long variants. Human tissues contain five isoforms of AKs, named AK1-AK5 (*2*). The AK1 and AK5 cytosolic isoforms are short variants (*3*), whereas mitochondrial AK2, AK3 (*4*), and AK4 are long variants. The subcellular localization of the AK4 is not determined yet (*5*). On behalf of these two classes, bacterial AKs, like the AK from *Mycobacterium tuberculosis*, are short variants with low similarity with the eukaryote cytosolic AKs and were considered to form a new family of short bacterial adenylate kinases (*6*).

Several three-dimensional structures of short cytosolic and long variants of AK have been solved by X-ray crystallography in the free and complexed form (*7*−*11*). All these AKs share a highly related tertiary structure (with an α/$\beta$ global fold), showing a central five-stranded parallel $\beta$-sheet surrounded by several α-helices (the CORE of the protein) and two peripheral domains, $AMP_{bd}$ and LID, which have a functional role in isolating the mononucleotide and the

[†] This work was supported by the Centre National de la Recherche Scientifique, the Institut National de la Santé et de la Recherche Médicale, the Institut Curie, the Institut Pasteur, and the European Community (TMR program). S.M. gratefully acknowledges a Marie-Curie postdoctoral fellowship from European Community. The 750 MHz spectra were recorded at the SON NMR Large Scale Facility in Utrecht, which is funded by the Access to Research Infrastructures program of the European Union (HPRI-CT-1999-00005 or HPRI-CT-2001-00172).

[‡] The atomic coordinates (code 1P4S) have been deposited in the Protein Data Bank (http://www.rcsb.org).

* To whom correspondence should be addressed. Tel: 33 1 69 86 31 63. Fax: 33 1 69 07 53 27. E-mail: (S.M.) Simona.Burlacu@curie.u-psud.fr; (C.T.C.) Gil.Craescu@curie.u-psud.fr.

[§] Centre Universitaire.

[||] Institut Pasteur.

[⊥] Present address: Unité de Chimie Organique (CNRS URA2128), Institut Pasteur, 28 rue du Dr. Roux, 75724 Paris Cedex 15, France.

[1] Abbreviations: AK, adenylate kinase; AKmt, adenylate kinase from *Mycobacterium tuberculosis*; AKe, adenylate kinase from *Escherichia coli*; AK1p, cytosolic muscle adenylate kinase from porc; AK1c, cytosolic muscle adenylate kinase from chicken; $AMP_{bd}$, the AMP binding domain; Ap5A, [$P^1$,$P^5$-bis(5′-adenosine)-pentaphosphate]; NMR, nuclear magnetic resonance; HSQC, heteronuclear single quantum coherence; $R_1$, longitudinal relaxation rate constant; $R_2$, transverse relaxation rate constant; NOE, nuclear Overhauser effect.

10.1021/bi0355995 CCC: $27.50 © 2004 American Chemical Society
Published on Web 12/09/2003

trinucleotide, respectively, from the solvent during the catalytic cycle (*12*). Another common trend of the AK enzymes is the ATP binding motif, called the P-loop (GXXGXGK, represented by residues 7−13 in AKmt), that binds the phosphates of ATP. The $AMP_{bd}$ is defined by two helices (α2 and α3), and the LID domain is a variable loop for the short forms and a four-stranded antiparallel β-sheet for the long ones. The length and structural organization of the LID domain is thus the main structural difference between the two classes. Comparison between free and complexed adenylate kinase structures shows that the peripheral domains, AMPbd and LID, undergo large movements during the catalytic cycle (*13*, *14*).

Nowadays, tuberculosis is still considered a major public health problem, due to the emergence of multiple drug-resistant strains and to the coinfection with HIV. AK is a key enzyme in the metabolism (*15*), and taking into account that its catalytic properties are different from the eukaryotic AKs (*6*), one can hypothesize that this bacterial enzyme could be a new target for antituberculosis drugs. A better understanding of the structure−function relationship of the AKmt is thus of great interest.

In the absence of any structural information on short bacterial AKs, one may ask whether the three-dimensional structure of these enzymes is similar to the other well-characterized AKs. In our previous studies (*6*), we proposed a structural model for AKmt (based on the NMR data and secondary structure prediction), but the presence of several deletions in the sequence (particularly in the region corresponding to the fifth β-strand) rendered uncertain the prediction of the C-terminal structural arrangement. In addition, it is now commonly accepted that understanding the functional mechanism, its modulation, and the structure-based drug design requires a structural resolution higher than the molecular modeling could actually produce.

The aim of the present work was the determination of the three-dimensional structure of AKmt at atomic resolution and investigation of its backbone internal dynamics. Analysis of structural and dynamic properties of AKmt provides a molecular basis for the explanation of significant enzymatic differences relative to other eukaryotic counterparts.

## MATERIALS AND METHODS

*Sample Preparation.* Uniformly labeled recombinant AKmt was overproduced in *Escherichia coli* strain Bli5/pHL20 (*6*) using M9 minimal medium containing 1.5 g/L 99% ($^{15}$N)-ammonium sulfate and 3.0 g/L 99% ($^{13}$C)-glucose as the sole nitrogen and carbon source, respectively, and supplemented with 100 μg/mL ampicillin and 30 μg/mL chloramphenicol. At an $OD_{600}$ of 1.2−1.4, the culture was induced by addition of isopropyl-β-D-thiogalactoside (1 mM final concentration) and further incubated at 37 °C for 16 h. The protein was purified as described earlier (*6*) by a two-step procedure. The purified AKmt was dialyzed extensively against ammonium bicarbonate (50 mM) and lyophilized.

*NMR Spectroscopy*. The NMR experiments were carried out on an Unity 500 MHz Varian spectrometer and on a Varian Inova 750 MHz spectrometer (European SON NMR Large-Scale Facility, Utrecht) at 308 K. The NMR samples at a concentration of 1.2 mM (pH 7.1) were obtained by dissolving the lyophilized protein in potassium phosphate buffer (50 mM) in 95% $^1H_2O$/5% $^2H_2O$ or in 100% $^2H_2O$. Proton chemical shifts were referenced relative to the water signal, which resonates at 4.69 ppm from the sodium 2,2-dimethyl-2-silapentane sulfonate (DSS) at 308 K. $^{15}$N and $^{13}$C references were set indirectly relative to DSS using the frequency ratio (*16*). The NMR data were processed and analyzed using Felix98 software (Accelrys, San Diego), running on a Silicon Graphics Indigo workstation.

The final size of the HSQC matrix was 1024 × 1024 real points. The data have been multiplied by exponential ($F_2$) and π/4 shifted sine-bell ($F_1$) functions before Fourier transformation. For the 3-D $^{15}$N TOCSY-HSQC and NOESY-HSQC spectra, the data were extended by linear prediction in the indirect dimensions, zero-filled, and multiplied by sine-bell functions shifted by π/4 before Fourier transformation. The ($^1$H, $^{15}$N) 3-D spectra were acquired with 8000 and 1500 Hz spectral width for $^1$H for $^{15}$N dimension, respectively. A total of 128 complex points in the $t_1$ dimension ($^1$H), 32 complex points in the $t_2$ ($^{15}$N) dimension, and 2048 complex points in the acquisition $t_3$ dimension were collected.

*Structure Determination and Analysis.* Proton−proton distance restraints were derived from peak intensities in the 3-D $^{15}$N NOESY-HSQC and from 2-D NOESY (in $^2H_2O$) experiments. Calibration of the peak intensities was done according to the known interproton distances in the secondary structural elements (*17*). The NOE restraints were classified in four classes: strong (1.8−3.0 Å), medium (3.0−3.8 Å), weak (3.8−5.0 Å), and very weak (5.0−6.0 Å). Moreover, the NOE restraints in secondary structure elements were imposed to fall into the classical ranges for helical segments (3.3−3.7 for $d_{\alpha N}(i,i+1)$, 4.2−4.6 for $d_{\alpha N}(i,i+2)$, 4.0−4.4 for $d_{NN}(i,i+2)$, and 2.6−3.0 for $d_{NN}(i,i+1)$) and for the β-strand structures (2.0−2.4 for $d_{\alpha N}(i,i+1)$). A number of hydrogen bonds involved in the secondary structural regions were also included as distance restraints by using an upper and lower distance of 2.2 and 1.8 Å for the H−O pairs and 3.3 and 2.7 Å for the N−O pairs.

The chemical shifts of the backbone nuclei ($^{13}C^{\alpha}$, $^{13}C^{\beta}$, $^1H^{\alpha}$, and $^{15}$N) were used in the computer program TALOS (*18*) to predict the backbone torsion Φ and Ψ angles. Only the individual predictions labeled "good" and residues located in the α-helix and β-strand regions were included in the structure calculation. For α-helix and β-strands, dihedral angle values of $\Phi = -60$ (±30°) and $\Psi = -30$ (±40°) and $\Phi = -130$ (±40°) and $\Psi = 135$ (±45°), respectively, were used.

The structure determination was performed using 1809 NOE distance restraints of which 484 were intraresidue, 592 were sequential, 423 were medium range, and 310 were long range (Table 1). An additional 159 distance restraints derived from hydrogen bonds and 191 dihedral restraints were used. The calculation of the structures was done using MD_Schedule protocol of Discover (Accelrys, San Diego) running on an SGI workstation. Starting from an initial extended conformation, 100 structures were generated using a simulated annealing approach, including a 30 ps high-temperature phase (at 1000 K), followed by a cooling phase (down to 300 K) of 8 ps, and final energy minimizations. The NOE distance restraints were used in this protocol with a force constant of 32 kcal $mol^{-1}$·$Å^{-2}$. Φ and Ψ dihedral angle restraints were applied with a force constant of 30 kcal $mol^{-1}$ $Å^{-2}$. Twenty final structures have been selected based on lowest energy and number of restraint violations (no distance

Table 1: Restraint and Structural Statistics for the 20 Best Solution Structures of AKmt

| | | |
|---|---|---|
| NOE restraints | 1809 | |
| intraresidue | 484 | 27% |
| sequential | 592 | 33% |
| medium range ($2 \leq \|i-j\| < 5$) | 423 | 23% |
| long range ($\|i-j\| \geq 5$) | 310 | 17% |
| hydrogen bond restraints | 159 | |
| dihedral angle restraints ($\Phi$,$\Psi$) | 191 | |
| average number of restraint violations | | |
| violations per structure (>0.5 Å) | none | |
| dihedral angle restraint violations (>10°) | none | |
| average rmsd. (Å) from the average structure | | |
| helices 1, 2, 3, 4, 5, 6, 7, 8, 9 and $\beta$-sheet[a] | 0.77 | |
| helices 1, 2, 3, 4, 5, 8, 9 and $\beta$-sheet[a] | 0.55 | |
| all atoms | 1.97 | |
| ensemble Ramachandran plot | | |
| residues in the most-favored region | 84.6% | |
| residues in additional allowed regions | 11.5% | |
| residues in generously allowed regions | 1.9% | |
| residues in disallowed regions | 1.9% | |

[a] Backbone atoms (N, C′, C$^a$).

violation larger than 0.5 Å and no dihedral violation greater than 10°). The final structures were analyzed using the InsightII and PROCHECK-NMR programs (*19*). The coordinates of the 20 best structures have been deposited in the Protein Data Bank, with the entry code 1P4S.

*Backbone Amide $^{15}N$ Relaxation Measurements.* The nuclear relaxation experiments were performed on an Unity 500 MHz Varian spectrometer at 308 K. The $^{15}N$ spin−lattice ($R_1$), and spin−spin ($R_2$) relaxation rate constants, as well as the NOE (steady-state {$^1H$}-$^{15}N$ nuclear Overhauser effect) were measured using sensitivity-enhanced pulse sequences with gradient selection provided by Kay et al. (*20*). The spectra were acquired with 8000 and 1500 Hz spectral widths, 2048 × 128 complex points in the $F_2$ and $F_1$ dimension, respectively, and eight transients per FID. To obtain resolution-optimized spectra, the time data were apodized with Lorentzian−Gaussian and sin$^2$ window functions in the $t_2$ and $t_1$ dimensions, respectively. The data were zero-filled to generate a 2048 × 512 real point matrixes. The $R_2$ values were obtained from 12 experiments with 10 relaxation delays: 15.7(×2), 31.4, 47.1, 62.8, 78.5, 94.2-(×2), 109.9, 125.6, 157, and 188.4 ms. The $R_1$ values were obtained from 11 experiments with nine relaxation delays: 10(×2), 80, 160, 250, 450(×2), 650, 800, 1000, and 1300 ms. The cross-peak intensities were evaluated as peak heights, and the uncertainties were determined from duplicate spectra and from the standard deviation of the base-plane noise. The $R_1$ and $R_2$ values were obtained by fitting the experimental data with a two parameter monoexponential equation. The heteronuclear {$^1H$}-$^{15}N$ NOE values were determined from the ratios of the intensities of the peaks in the spectra acquired in the absence and presence of proton saturation.

*Determination of the Overall Rotational Correlation Time.* The global rotational correlation time $\tau_c$ of the molecule was estimated using a recent approach (*21*) designed to minimize the effects of the slow motions. From the $R_1$ and NOE values (less affected by the slow motions) obtained for amides in the secondary structure elements and using an arbitrary value for $\tau_c$, the $R_2$ values were calculated and compared with the experimental data. The $\chi^2$ for $R_2$ (summed over the selected sites) as a function of $\tau_c$ shows a minimum that indicates the best estimate of $\tau_c$.

*$^{15}N$ Relaxation Analysis.* To describe the motion of the backbone $^1H$-$^{15}N$ vector (from $R_1$, $R_2$, and NOE relaxation data), we used the Lipari and Szabo (*22*, *23*) model-free approach where the spectral density function $J(\omega)$ of the amide vector is expressed as

$$J(\omega) = 2/5[S^2\tau_c/(1 + \omega^2\tau_c^2) + (1 - S^2)\tau/(1 + \omega^2\tau^2)]$$

where $1/\tau = 1/\tau_e + 1/\tau_c$, $\tau_e$ is the correlation time for fast internal motion, $\tau_c$ is the global rotational correlation time, and $S^2$ is the generalized order parameter that is the measure of the degree of spatial restriction of the vector fast motion. It ranges from 0 to 1, with 0 indicating unrestricted internal motions and 1 completely restricted internal motions.

An extended model-free spectral density function was proposed (*24*) for cases where internal motions occur on two different time scales

$$J(\omega) = 2/5[S^2\tau_c/(1 + \omega^2\tau_c^2) + (1 - S_f^2)\tau'_f/(1 + \omega^2\tau'^2_f) + (S_f^2 - S^2)\tau'_s/(1 + \omega^2\tau'^2_s)]$$

where order parameter $S^2 = S_s^2S_f^2$. $S_s$ and $S_f$ describe the order parameter for slow (nanosecond) and fast (subnanosecond) internal motions, respectively. $\tau_f' = \tau_f\tau_c/(\tau_f + \tau_c)$ and $\tau_s' = \tau_s\tau_c/(\tau_s + \tau_c)$, where $\tau_f$ is the correlation time for internal motion on a fast time scale and $\tau_s$ is the correlation time for internal motion on a slower time scale.

## RESULTS AND DISCUSSION

*NMR Analysis.* Almost complete $^1H$, $^{13}C$, and $^{15}N$ resonance assignment of the AKmt spectra was obtained using double-labeled $^{15}N/^{13}C$ samples and heteronuclear spectroscopic experiments at 308 K (*25*). Resonances corresponding to residues G12-T15 that belong to the ATP binding P-loop were not observed in NMR spectra and remained unassigned. The combined analysis of secondary chemical shifts of $^1H^\alpha$, $^{13}C^\alpha$, and $^{13}C^\beta$ nuclei (*26*) and of short and medium range NOEs (*17*) enabled us to locate the secondary structure elements along the sequence. The protein contains nine α-helices: $\alpha_1$ (16−23), $\alpha_2$ (33−41), $\alpha_3$ (46−54), $\alpha_4$ (62−71), $\alpha_5$ (92−102), $\alpha_6$ (117−124), $\alpha_7$ (135−144), $\alpha_8$ (148−159), and $\alpha_9$ (170−178) and five $\beta$-strands: $\beta_1$ (2−6), $\beta_2$ (28−30), $\beta_3$ (81−84), $\beta_4$ (109−114), and $\beta_5$ (160−164). The $\beta_5$ strand is one residue shorter than in *E. coli* AK but has the same length as in AK1. Identification of the interstrand long range NOEs between backbone protons $d_{NN}(i,j)$ and $d_{\alpha N}(i,j)$ enabled us to define unambiguously the five-stranded parallel $\beta$-sheet topology.

*Three-Dimensional Structure.* The structure was calculated using a simulated annealing protocol under the Discover (cvff) force field, based on 1809 NOE restraints and 191 dihedral angle restraints. The final 20 structures of AKmt, shown in Figure 1A, were chosen for their low total potential energy and best agreement with the experimental restraints. The corresponding restraint and structural statistics are given in Table 1. The root-mean-square deviation (RMSD) for the best superposition of the 20 final structures is 0.77 and 1.97 Å when using the backbone heavy atoms in regular structural elements or all the atoms, respectively. The regularity of the

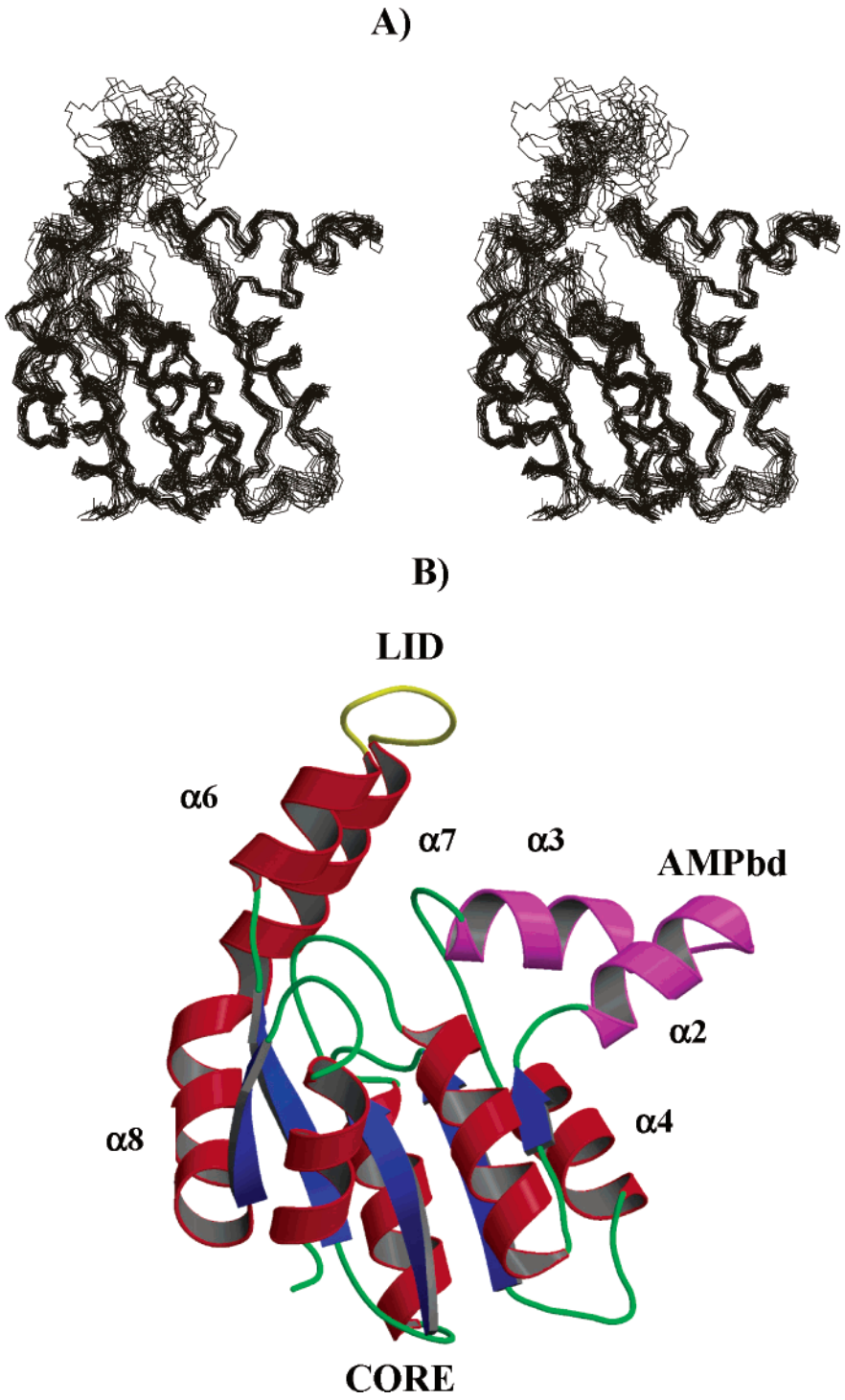


FIGURE 1: (A) Stereoview of the best superposition of the final 20 structures of AKmt using the backbone atoms (N, C′, and $C^{\alpha}$) in secondary structural elements (with the exception of helices α6 and α7). (B) Ribbon diagram of the tertiary structure of the AKmt, represented using the best structure in the ensemble and the MOLSCRIPT software (*53*). The LID and the AMPbd domains are in yellow and magenta, respectively. Secondary structure elements are in blue (the *β*-sheet) and in red (the α-helices).

protein conformations was assayed using the PROCHECK-NMR program (*19*). More than 84.6% of the Φ and Ψ angles in all structures were found in the most favored regions of the Ramachandran plot, 11.5% of the angle pairs correspond to additional allowed regions, and 1.9% were placed in generously allowed regions.

In agreement with the distribution of the NOE restraints along the sequence, the structure of some protein regions is less defined, as reflected in the backbone atom RMSD values relative to the average structure (Figure 2). The residues in the segments A11-G14, P60−S61, G166-D169, and G126-A130 (the LID loop) display few NOEs as compared to the other structural elements. The LID and the helices $\alpha_6$ and $\alpha_7$ that anchor the LID domain to the CORE of the protein are less defined due to a lower number of long range NOE restraints. No detectable contacts with the CORE of the protein were observed for the LID domain (excepting the linkers $\alpha_6$ and $\alpha_7$), and this explains the poor precision of its spatial orientation. The poor definition of the peripheral domain, together with the connecting helices, is well-

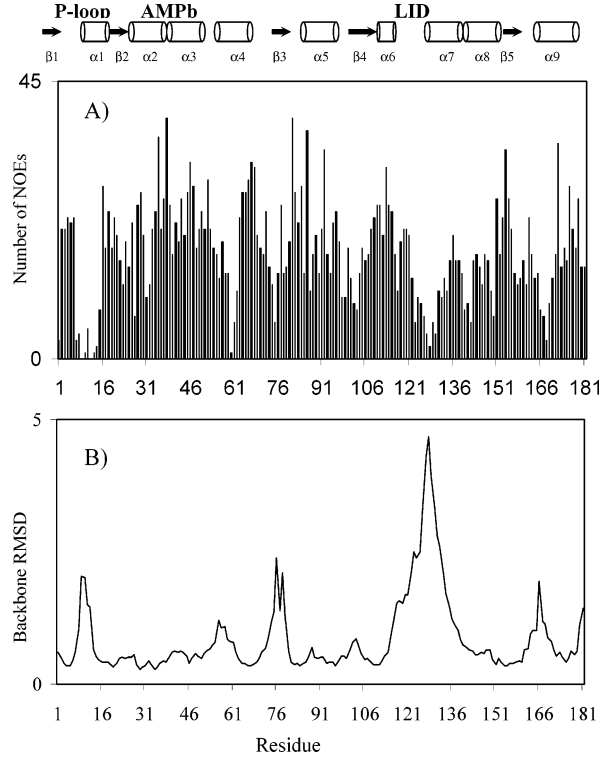


FIGURE 2: (A) Distribution of NOEs used in AKmt structure calculation as a function of residue number. (B) Distribution of the backbone RMSD for the 20 NMR solution structures with respect to the average coordinates.

illustrated by the fact that the RMSD for the backbone heavy atom coordinates in secondary structure elements improves considerably (from 0.77 to 0.55 Å) when helices $\alpha_6$ and $\alpha_7$ are ignored.

Similarly to other AKs, AKmt is a globular protein with an $\alpha/\beta$ fold organized into three domains: CORE, AMPbd, and LID (Figure 1B). The CORE domain representing the main scaffold of the structure includes the five-stranded parallel $\beta$-sheet (in blue), surrounded by helices $\alpha_1$ and $\alpha_4-\alpha_9$ (in red). The $\alpha_2$ and $\alpha_3$ helices (in magenta) and their connecting loops define the AMPbd domain, spanning residues T31 to V59. As in the short cytosolic vertebrate variants (AK1), the LID domain is reduced to only 10 residues (K125-D134), forming a highly flexible loop (in yellow).

*Backbone Internal Dynamics.* Nuclear $^{15}$N relaxation data were analyzed for 149 backbone amide groups of the 174 nonproline residues of AKmt. Amide resonances corresponding to the ATP binding P-loop (G10-K13) and to neighboring residues (G14, T15, Q16, A17, and K19) were not observed in the HSQC spectrum, probably due to an intermediate exchange (on the NMR time scale) between several conformations in the absence of any bound ligand (*27*). It is worth noting that the corresponding residues in AK1c remained unassigned even in the presence of the strong inhibitor Ap5A (*28*), suggesting that the substrate binding in this region does not change dramatically the dynamics behavior. In addition, the amide protons of residues R129 and A130 (from the LID domain) as well as T31, S61, S116, and M168, which belong to loop regions and are highly exposed to the solvent, may have a fast exchange with water protons, explaining their absence from the HSQC spectrum. We should mention that, due to solubility problems, the assignment as well as the structural and dynamical analysis were performed at pH 7.1, where the amide proton exchange is considerably increased. In compensation, working at a more physiological pH allows a more reliable comparison between the structural and the dynamic properties studied here and the biological function. Finally, for peak superposition reasons, the cross-peaks corresponding to Y86, E98, L120, L124, K125, I137, V143, D146, V165, and E170 could not be accurately quantified and were not taken into account in the dynamics analysis. $^{15}$N longitudinal relaxation rate constants ($R_1$), $^{15}$N transverse relaxation rate constants ($R_2$), and $\{^1$H-$^{15}$N$\}$ heteronuclear NOE values for the remaining amide groups in AKmt are plotted as a function of the residue number in Figure 3. The $R_1$ and $R_2$ profiles are relatively uniform along the sequence. Except G7, which is close to the P-loop region, the measured $R_1$ and $R_2$ values are within the range 1.2−2.1 and 7.0−16.6 $s^{-1}$, respectively. Larger deviations from the mean values (1.6 and 11.0 $s^{-}$,[1] respectively), associated with a significantly increased uncertainty, are observed around the P-loop, the LID domain, as well as in the $\alpha3/\alpha4$ and $\beta5/\alpha9$ loops. The heteronuclear $\{^1$H-$^{15}$N$\}$ NOE values, which are very sensitive to the high-frequency internal motions, are grouped around 0.6, with very small values (down to 0.2) in the LID domain. The second helix of the AMPbd domain and the consecutive loop show higher internal dynamics in the picosecond time scale, relative to the residues in the CORE of the protein, but smaller than for the residues in the LID domain. This suggests that rapid local motions in the AMPbd domain are less effective than in the LID domain. This is in contrast with the dynamics of the AKe in the free-form (*29*, *30*), for which the $\{^1$H-$^{15}$N$\}$ NOE data indicate that the rapid motions are comparable in the two domains.

Atomic coordinates from the best of the final 20 NMR structures were used to calculate the relative ratio of the principal components of the inertia tensor: 1.00:0.83:0.74. The result shows that the protein is roughly spherical, suggesting that its overall rotation is only slightly anisotropic. To confirm this hypothesis, we used the relaxation ratio $R_2/R_1$ to test whether axially symmetric or fully anisotropic tumbling models may give a better fit to the experimental data than the isotropic model. The TENSOR program (*31*), having the atomic coordinates of AKmt and the $R_2/R_1$ ratio for the residues located in secondary structural elements (that are assumed to be more rigid) as inputs, was employed to evaluate the relative reliability of various rotational models (*32*). The axially symmetric and fully anisotropic rotational diffusion tensor models give no statistically significant improvement in the $\chi^2$ value over the isotropic model. The latter model was thus retained as a good description for the overall motion of the molecule.

The second step in the analysis of the $^{15}$N relaxation data under the Lipari and Szabo formalism was the determination of the overall rotational correlation time $\tau_c$ of AKmt. From the $R_2/R_1$ ratio (*33*, *34*), $\tau_c$ was initially estimated to be 8.74 ± 0.02 ns. To minimize the effect of eventual slow exchange processes, a second procedure (*21*) was equally used to estimate the $\tau_c$. The value thus obtained was 9.19 ± 0.05 ns, which is close to the previous estimation and agrees quite well with the molecular size and isotropy of the protein. According to this value, AKmt appears to be more compact than the ligand-free AKe ($\tau_c$ = 15.1 ns) and closer to the shape of the Ap5A-bound AKe ($\tau_c$ = 11.6 ns) (*35*). It is

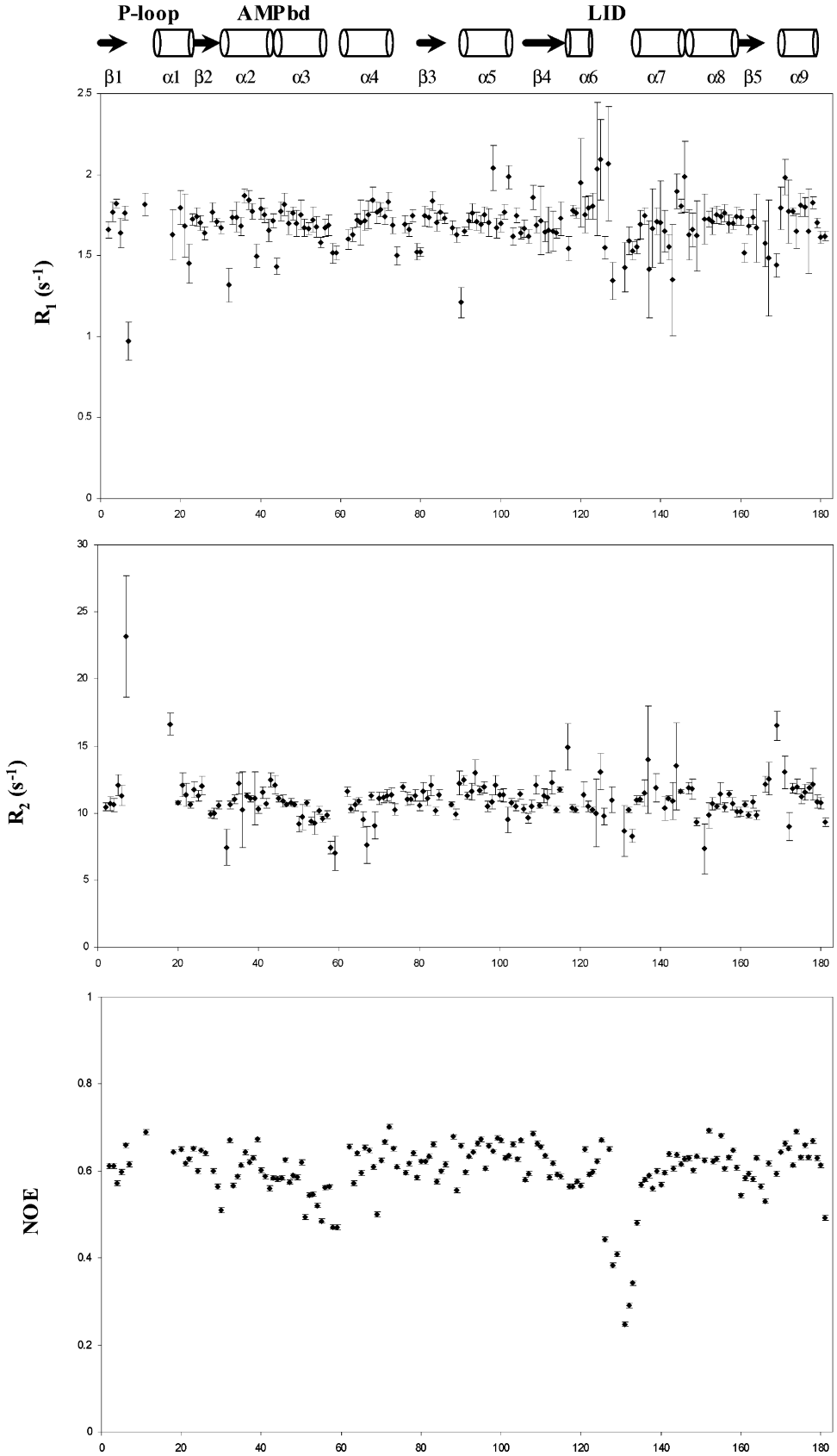


FIGURE 3: $^{15}N$ $R_1$, $R_2$, and NOE relaxation parameters, obtained at 500 MHz $^1H$ Larmor frequency and 308 K, plotted as a function of the residue number of AKmt. The secondary structure elements of the protein are also indicated.

worth noting that an alternative analysis of the $^{15}N$ relaxation data in AKe uncovered a much shorter correlation time (at the nanosecond time scale) for the two domains involved in catalysis (*35*).

With this last estimation for the global correlation time, we used the Lipari and Szabo model-free approach (*22*, *23*) to derive the microdynamic parameters. In a simpler approach, we considered only three microdynamical parameters

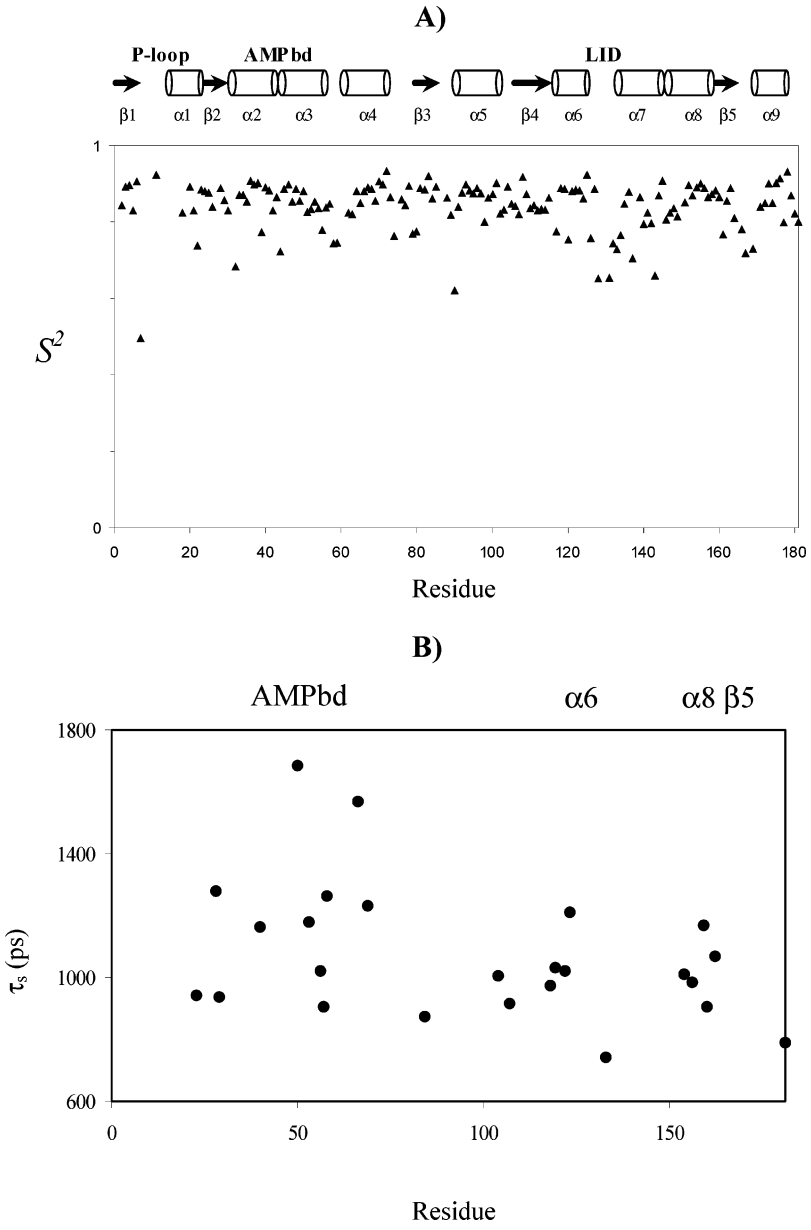


FIGURE 4: (A) Order parameters ($S^2$) of the backbone H−N vectors in AKmt. The secondary structure elements, defined by the present NMR experiments, are indicated at the top of the figure. (B) Effective correlation time ($\tau_s$) for slower internal motions for AKmt.

(the order parameter $S^2$, the internal correlation time $\tau_e$, and the exchange contribution $R_{ex}$), assuming that the time constant of the fast motions is much smaller than the global correlation time. The obtained generalized order parameter, $S^2$, is plotted as a function of the residue number in Figure 4A. Mean $S^2$ values calculated for each secondary structural element vary between 0.82 and 0.89, falling in a range typical for the well-defined secondary structure of proteins (*36*). Similar order parameters $S^2$ were found for the free-form AKe (*29*). $\beta$2, α2, α4, $\beta$3, α5, α6, α8, and α9 exhibit more homogeneous order parameters, while α3 (the second half), $\beta$4, α7, and $\beta$5 have systematically lower values. The amplitude of the fast internal motions (inversely proportional to $S^2$) is significantly higher in the loops connecting the secondary structural elements and especially in the LID and $\beta$5/α9 loops. Particularly lower $S^2$ values (down to 0.64) were noted in the loop representing the LID domain, significantly smaller relative to the corresponding values in apo-AKe (*29*). This means that the fast internal motions in this domain are less restricted as compared with the LID fragment of the AKe. It should be noted that this domain is larger in AKe and includes a four-stranded antiparallel $\beta$-sheet, while in AKmt it is represented by a small 10 residue loop. Some residues (G7, L58, V59, V90, G166, T167, D169) belonging to the two nucleotide binding sites of the protein also exhibit a higher amplitude fast motion ($S^2$ values under 0.8), probably related to the functional role that these residues play in the catalytic process.

Unusually, the residues in the C- and N-terminal ends of the AKmt display a similar amplitude of the fast movement as the residues in α-helical and $\beta$-strand elements. The restrained movement of these segments should be correlated with their well-defined structure and multiple van der Waals contacts with the protein CORE.

In the case of 17 residues (G7, I26, K44, N79, V90, E91, K94, M99, E117, R127, G128, D134, I137, R140, G166, T167, and M169), it was noted that the exchange contribution $R_{ex}$, which represents an additional contribution to the

transverse relaxation rate, takes significant higher positive values relative to the majority of the residues ($1-2\ s^{-1}$). This parameter reflects particular movements of the protein backbone on a much slower time scale (microseconds to milliseconds) and is usually conceived as local or regional conformational exchanges or aromatic side chain flipping. The largest $R_{ex}$ term ($16.6\ s^{-1}$) corresponds to G7, the only residue in the P-loop observable in HSQC spectra. Together with broadened NMR signals coming from contiguous residues (G10-K13) in the ATP binding loop, this suggests strongly that the P-loop region displays conformational motions on the slower time scale. Similar conclusions could be drawn for some residues in the LID and $\beta$5/$\alpha$9 loops (R127, G128, D134 and G166, T167, M169, respectively) that are involved in binding or protecting the phosphate donor (ATP). High $R_{ex}$ terms were also noted for three other residues belonging to the $\beta$4/$\alpha$6 loop, helix $\alpha$7, and helix $\alpha$8 (E117, 5.3; R140, 7.7; and M168, 7.2 $s^{-1}$, respectively). Their localization in the three-dimensional structure shows that they also belong to the cavity harboring ATP. We can therefore conclude that various structural elements playing key roles in the trinucleotide binding display slow conformational dynamics that could be relevant for the enzyme function.

Relaxation parameters were also analyzed in the frame of an extended approach (*24*) that takes into account additional slower internal motions, on the order of magnitude of the global rotational diffusion time. Two order parameters are now considered, $S_f^2$ for the fast picosecond internal motions and $S_s^2$ for slower nanosecond time scale internal motions (faster than $1/\tau_c$ but slower than $1/\tau_e$), characterized by the correlation time $\tau_s$. For simplification, the exchange term is considered to be negligible in this case. The selection of the residues for which the extended model-free approach is more appropriate was performed using Monte Carlo simulations. Twenty-five residues (Figure 4B) of AKmt (for which the experimental data were in the 95% confidence limits of the model) exhibit slow motions on the nanosecond time scale, with correlation times between 0.75 and 1.68 ns. They are essentially associated with the AMPbd domain, the $\alpha$6 helix, and the contiguous C-terminal $\alpha$8 helix and $\beta$5 strand. The $S_s^2$ values are slightly lower than $S_f^2$ for all these residues, indicating that the backbone flexibility is largely determined by the nanosecond motions.

In conclusion, the internal dynamics analysis showed that the well-structured backbone of apo-AKmt is animated by several type of motions, at various time scales from picoseconds to milliseconds. In the fast movement regime, the larger amplitudes are associated almost exclusively with the LID domain, while the nanosecond mobility is rather associated with the AMPbd domain. The slower movements, detected in the ATP binding region, could be related to the functional role of the corresponding segments in the recognition and reversible binding of the trinucleotides.

*Biological Implications.* As shown by MULTALIN multiple sequence alignment (*37*), AKmt exhibits 45% sequence identity with AKe and about 30% identity with the cytosolic chicken (AK1c) or porcine (AK1p) adenylate kinases (Figure 5). The loops $\alpha$6/$\alpha$7 and $\alpha$8/$\beta$5 are four and two residues shorter, respectively, than in the short forms (AK1c and AK1p). In addition, a four residue insertion may be noted between $\alpha$5 and $\beta$4 in AKmt. The *E. coli* enzyme has a remarkably longer LID domain (27 more residues than AK1) and additional five residues relative to AK1 between $\alpha$8 and $\beta$5. Despite this important sequence variation, comparison of the present NMR structure with the available X-ray structures (*7*−*9*, *38*−*40*) shows that the secondary structure elements and their tertiary assembly are well-conserved. Superposition of the present NMR structure of AKmt to AKe and AK1p, using the heavy backbone atoms in the CORE secondary segments, gives an RMSD of 2.4 and 3.7 Å, respectively. Inclusion of the two $\alpha$-helices ($\alpha$2 and $\alpha$3) that define the AMPbd domain results in a degradation of the structural fit: RMSD rises up to 4.1 and 4.3 for AKe and AK1p, respectively. It is readily observed that the AMPbd domain in AKmt is in closer contact with the CORE of the protein as compared to AKe and AK1 free-forms (Figure 6). Comparative analysis of X-ray structures of AKe in apo and holo forms revealed that the AMPbd helices and especially the LID domain undergo large spatial movements upon ligand binding (*7*). Surprisingly, when the three-dimensional structure of AKmt (CORE and AMPbd) is superimposed to the structure of the AKe in complex with Ap5A (a bisubstrate analogue), the RMSD goes down from 4.1 to 2.6 Å, indicating that the relative position of the mononucleotide binding domains in apo AKmt are rather similar to that observed in the holo state of other AKs.

The decreased accessibility for the mononucleotides in the AKmt should have significant consequences on the catalytic parameters, particularly in relation to the corresponding values in other bacterial or eukaryotic enzymes. Indeed, the apparent $K_m$ of AKmt for AMP, measured at 30 °C and pH 7.4 (*6*), is about 5 times greater than for ATP, while the corresponding parameters are almost equal in AK1 and AKe. This difference is mainly due to a significant increase of the $K_m$ value for AMP in AKmt relative to AKe and AK1 (by 5.5 and 2.4 times, respectively). Therefore, the catalytic properties reflect a significantly decreased affinity for the mononucleotide in the pathogenic bacteria.

Loop or domain motions are widely recognized as key elements in the catalytic mechanism of many enzymes. Usually, these relatively flexible structural segments contribute to the creation of a kind of tunnel, directing the substrates from the solvent to the active site, and then, by subsequent catalysis-coupled movements, they close the cavity and isolate the reactive intermediates from the solvolysis (*41*). A more rigid or persistently closed conformation of the active site cavity could slow the kinetic $k_{on}$ constant of the substrate binding or over-stabilize the transition state, thus decreasing the enzymatic efficiency (*42*−*44*). The closer conformation of the AMPbd domain and its reduced amplitude for the fast motion components in AKmt may synergistically act toward the decreased catalytic activity relative to other known AKs.

The more compact structure of AKmt provides also a structural explanation of the relative structural stabilities, observed in various AKs (*6*, *45*). Experimental observations indicated that the midpoint ($T_m$) of the heat-induced cooperative transition of apo AKmt (64.8 °C) is 12 °C higher than that of AKe (52.5 °C), closer to the value observed with AKe/Ap5A complex (61.1 °C). While Ap5A shifts the $T_m$ value for AKe by 9 °C, it shows only a marginal effect on AKmt (2 °C) (*6*). This is in agreement with the previous

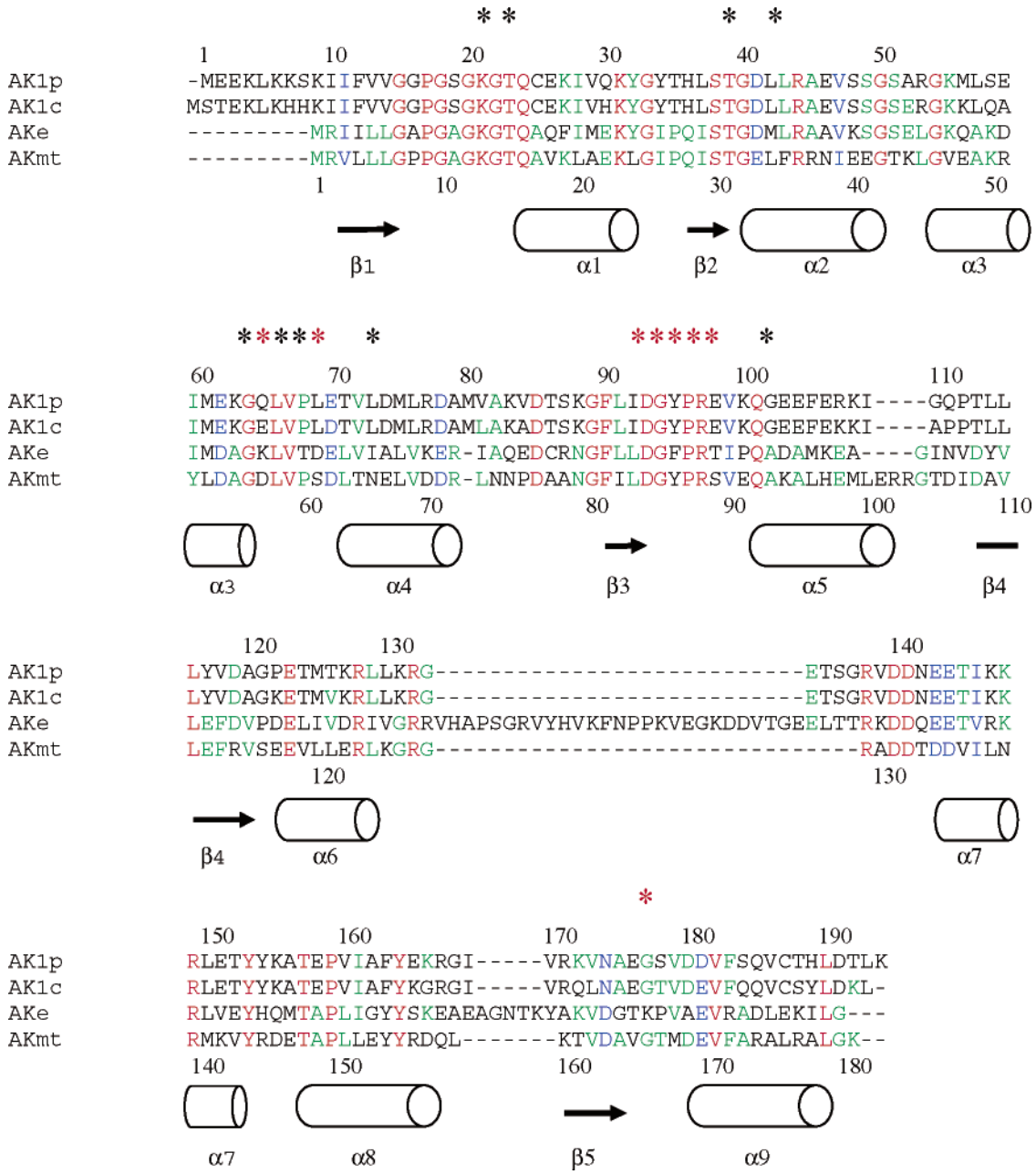


FIGURE 5: Sequence of AKmt aligned to the AKe and cytosolic muscle adenylate kinases (AK1p from porc and AK1c from chicken). The secondary structure of AKmt derived from the NMR data is indicated on the bottom of the sequences. The residues found to play an important role in the catalytic function of the AK1c and AKe are indicated by a black and red star, respectively.

structural comparison showing that AKmt is more compact than AKe in the free form and is more similar to the AKe/Ap5A complex. As the short form AK1 or the AKe construct lacking the LID domain (*46*) do not exhibit high thermal stability, we can assume that the AMPbd domain, and its position relative to the protein CORE, play an important role in the structural stability of mononucleotide kinases.

The validity of the previous analysis of the structure/stability/function relationships among AK of various origins requires an assessment of sequence differences and their eventual consequences on the catalytic activity. Site-directed mutagenesis (*47*, *48*), NMR (*28*), and X-ray studies (*9*) of the AK complexes provided a wealth of information allowing the identification and characterization of the residues playing a critical functional role, mainly in AMP/ATP binding and phosphate transfer. Among the residues lying around the ATP moiety, only T23 (conserved in AKmt) was shown to have NOE contacts with the adenine ring in AK1c/Ap5A complex (*28*), but its role is thought to be rather related to the interaction with α-phosphoryl group. Another close residue, K21 (K13 in AKmt), plays a critical role in the catalytic process and is involved in the proper orientation of the *β*-phosphate group of MgATP (*48*). Many more residues were found to interact with the AMP moiety. Studies on AK1c showed that L66 and V67 form a hydrophobic cap, in interaction with the adenine ring of AMP (*47*). These highly conserved residues correspond to L58 and V59 in AKmt. Other residues, like T39, L43, G64, V72, and Q101 (*28*) were shown to have NOE contacts with the adenine or sugar protons of AMP. The side chains in corresponding positions in AKe (Figure 5) show also multiple contacts with the mononucleotide, as shown by the analysis of the crystallographic structure of the complex AKe/Ap5A (*9*). Therefore, in contrast with ATP, the adenosine of the AMP

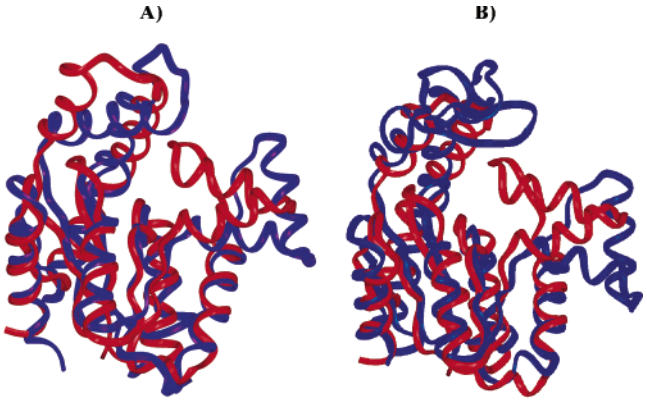


FIGURE 6: Ribbon representation of the best NMR structure of AKmt (in red) superimposed on the crystal structure of cytosolic muscle adenylate kinase AK1p (A) and on the crystal structure of AKe (B) (in blue). The superposition was optimized using the backbone atoms (N, C′, $C^{\alpha}$) in the secondary structure elements of the CORE of the proteins.

exhibits more interactions with the enzyme, an observation that could be related to the higher specificity for the nucleotide monophosphates. Site-directed mutagenesis experiments and enzymatic assays (*46*, *49*−*52*) also revealed that residues belonging to the D84-R88 fragment of AKe are critically involved in maintaining the structural integrity and/or the catalytic function of the protein. This segment, as well as the individual side chains mentioned earlier, is highly conserved in all known isoforms of AKs, including AKmt. Therefore, conformational factors, as those controlling the accessibility to the AMP binding pocket revealed by the present work, rather than sequence alterations, should explain the difference in enzymatic parameters of the pathogenic bacteria.

*Conclusion*. The results presented in this paper represent the first structure of an AK from a pathogenic bacterium. The high-resolution structure obtained in solution and at physiologically relevant pH provides a useful structural basis for understanding the specific functional properties of the enzyme and for the exploration of possible specific inhibitors. The present analysis suggests that the AMP binding domain plays a determinant role in the catalysis and structural stability of the protein. Further NMR analysis of the AKmt in complex with the bisubstrate analogue Ap5A will provide a deeper insight into the substrate-induced conformational changes and intermolecular contacts.

## ACKNOWLEDGMENT

We thank Rainer Wechselberger for spectra acquisition on the 750 MHz spectrometer and Joël Mispelter for his help in relaxation data analysis. Helpful discussions with Dr. Octavian Bârzu and Gilles Labesse are acknowledged.

## REFERENCES

1. Noda, L. H. (1973) Adenylate kinase, in *The Enzymes* (Boyer, P. D., Ed.) 3rd ed., Vol. 8, pp 279−305, Academic Press, New York.
2. Van Rompay, A. R., Johansson, M., and Karlsson, A. (2000) Phosphorylation of nucleosides and nucleoside analogues by mammalian nucleoside monophosphate kinases, *Pharmacol. Ther. 87*, 189−198.
3. Van Rompay, A. R., Johansson, M., and Karlsson, A. (1999) Identification of a novel human adenylate kinase: cDNA cloning, expression analysis, chromosome localization and characterization of the recombinant protein, *Eur. J. Biochem. 263*, 12391−12396.
4. Fukami-Kobayashi, K., Nosaka, M., Nakazawa, A., and Gö, M. (1996) Ancient divergence of long and short isoforms of adenylate kinase: molecular evolution of the nucleoside monophosphate kinase family, *FEBS Lett. 385*, 214−220.
5. Yoneda, T., Sato, M., Maeda, M., and Takagi, H. (1998) Identification of a novel adenylate kinase system in brain: cloning of the fourth adenylate kinase, *Mol. Brain Res. 62*, 187−195.
6. Munier-Lehmann, H., Burlacu-Miron, S., Craescu, C. T., Mantsch, H. H., and Schultz, C. P. (1999) A new subfamily of short bacterial adenylate kinases with the *Mycobacterium tuberculosis* enzyme as a model: a predictive and experimental study, *Proteins: Struct., Funct., Genet. 36*, 238−248.
7. Müller, C. W., Schlauderer, G. J., Reinstein, J., and Schultz, G. E. (1996) Adenylate kinase motions during catalysis: an energetic counterweight balancing substrate binding, *Structure 4*, 147−156.
8. Müller, C. W., and Schultz, G. E. (1988) Structure of the complex of adenylate kinase from *Escherichia coli* with the inhibitor P1, P5-di(adenosine-5′-)pentaphosphate, *J. Mol. Biol. 202*, 909−919.
9. Müller, C. W., and Schultz, G. E. (1992) Structure of the complex between adenylate kinase from *Escherichia coli* and the inhibitor Ap5A refined at 1.9 Å resolution: a model for a catalytic transition state, *J. Mol. Biol. 224*, 159−177.
10. Abele, U., and Schulz, G. E. (1995) High-resolution structures of adenylate kinase from yeast ligated with inhibitor Ap5A, showing the pathway of phosphoryl transfer, *Protein Sci. 4*, 1262−1271.
11. Wild, K., Grafmüller, R., Wagner, E., and Schulz, G. E. (1997) Structure, catalysis and supramolecular assembly of adenylate kinase from maize, *Eur. J. Biochem. 250*, 326−331.
12. Yan, H., and Tsai, M. D. (1999) Nucleoside monophosphate kinases: structure, mechanism, and substrate specificity, *Adv. Enzymol. Relat. Areas Mol. Biol. 73*, 103−134.
13. Schulz, G. E., Müller, C. W., and Diederichs, K. (1990) Induced-fit movements in adenylate kinases, *J. Mol. Biol. 213*, 627−630.
14. Gerstein, M., Schultz, G., and Chothia, C. (1993) Domain closure in adenylate kinase. Joints on either side of the two helices close like neighboring fingers, *J. Mol. Biol. 229*, 494−501.
15. Kohiyama, M., Cousin, D., Ryter, A., and Jacob, F. (1966) Mutants thermosensible d'*Escherichia coli* K12. Isolement et caractérisation rapide, *Ann. Inst. Pasteur 110*, 465−486.
16. Wishart, D. S., Bigam, C. G., Yao, J., Abildgaard, F., Dyson, H. J., Oldfield, E., Markley, J. L., and Sykes, B. D. (1995) $^{1}H$, $^{13}C$, and $^{15}N$ chemical shift referencing in biomolecular NMR, *J. Biomol. NMR 6*, 135−140.
17. Wüthrich, K. (1986) *NMR of proteins and nucleic acids*, Wiley, New York.
18. Cornilescu, G., Hu, J.-S., and Bax, A. (1999) Identification of the hydrogen bonding network in a protein by scalar coupling, *J. Am. Chem. Soc. 121*, 2949−2950.
19. Laskowski, R. A., Rullmann, J., Antoon, C., MacArthur, M. W., Kaptein, R., and Thornton, J. M. (1996) AQUA and PROCHECK-NMR: Programs for checking the quality of protein structures solved by NMR, *J. Biomol. NMR 8*, 477−486.
20. Farrow, N. A., Muhandiram, R., Singer, A. U., Pascal, S. M., Kay, C. M., Gish, G., Shoelson, S. E., Pawson, T., Forman-Kay, J. D., and Kay, L. E. (1994) Backbone dynamics of a free and phosphopeptide-complexed Src homology 2 domain studied by $^{15}N$ NMR relaxation, *Biochemistry 33*, 5984−6003.
21. Mispelter, J., Izadi-Pruneyre, N., Quiniou, E., and Adjadj, E. (2000) Simple and accurate determination of global $\tau_R$ in proteins using $^{13}C$ or $^{15}N$ relaxation data, *J. Magn. Reson. 143*, 229−232.
22. Lipari, G., and Szabo, A. (1982) Model-free approach to the interpretation of Nuclear magnetic Resonance Realaxation in Macromolecules. 2. Analysis of experimental results, *J. Am. Chem. Soc. 104*, 4559−4570.
23. Lipari, G., and Szabo, A. (1982) Model-free approach to the interpretation of Nuclear Magnetic Resonance relaxation in macromolecules. 1. Theory and range of validity, *J. Am. Chem. Soc. 104*, 4546−4559.
24. Clore, G. M., Szabo, A., Bax, A., Kay, L. E., Driscoll, P. C., and Gronenborn, A. M. (1990) Deviations from the simple two-parameter model-free approach to the interpretation of nitrogen-15 nuclear magnetic relaxation of proteins, *J. Am. Chem. Soc. 112*, 4989−4991.
25. Miron, S., Munier-Lehmann, H., and Craescu, C. T. (2001) $^{1}H$, $^{13}C$ and $^{15}N$ resonance assignment and secondary structure of *Mycobacterium tuberculosis* adenylate kinase, *J. Biomol. NMR 19*, 89−90.

26. Wishart, D. S., and Sykes, B. D. (1994) The $^{13}C$ chemical-shift index: a simple method for the identification of protein secondary structure using $^{13}C$ chemical-shift data, *J. Biomol. NMR 4*, 171−180.
27. Burlacu-Miron, S., Perrier, V., Gilles, A.-M., Mispelter, J., Bârzu, O., and Craescu, C. T. (1999) $^{1}H$, $^{13}C$ and $^{15}N$ backbone assignment of *Escherichia coli* adenylate kinase, a 23.6 kDa protein, *J. Biomol. NMR 13*, 93−94.
28. Byeon, I.-J. L., Yan, H., Edison, A. S., Moobery, E. S., Abildgaard, F., Markley, J. L., and Tsai, M.-D. (1993) Mechanism of adenylate kinase. $^{1}H$, $^{13}C$, and $^{15}N$ NMR assignment, secondary structures, and substrate binding sites, *Biochemistry 32*, 12508−12521.
29. Shapiro, Y. E., Sinev, M. A., Sineva, E. V., Tugarinov, V., and Meirovitch, E. (2000) Backbone dynamics of *Escherichia coli* adenylate kinase at the extreme stages of the catalytic cycle studied by $^{15}N$ NMR relaxation, *Biochemistry 39*, 6634−6644.
30. Shapiro, Y. E., Kahana, E., Tugarinov, V., Liang, Z., Freed, J. H., and Meirovitch, E. (2002) Domain flexibility in ligand-free and inhibitor-bound *Escherichia coli* adenylate kinase based on a mode-coupling analysis of $^{15}N$ spin relaxation, *Biochemistry 41*, 6271−6281.
31. Dosset, P., Hus, J.-C., Blackledge, M., and Marion, D. (2000) Efficient analysis of macromolecular rotational diffusion from heteronuclear relaxation data, *J. Biomol. NMR 16*, 23−28.
32. Tjandra, N., Feller, S. E., Pastor, R. W., and Bax, A. (1995) Rotational diffusion anisotropy of human ubiquitin from $^{15}N$ NMR relaxation, *J. Am. Chem. Soc. 117*, 12562−12566.
33. Kay, L. E., Torchia, D. A., and Bax, A. (1989) Backbone dunamics of proteins as studied by $^{15}N$ inverse detected heteronuclear NMR spectroscopy: application to staphylococcal nuclease, *Biochemistry 28*, 8972−8979.
34. Palmer, A. G., Rance, M., and Wright, P. E. (1991) Intramolecular motions of a zinc finger DNA-binding domain from Xfin characterized by proton-detected natural abundance $^{13}C$ heteronuclear NMR spectroscopy, *J. Am. Chem. Soc. 113*, 4371−4380.
35. Tugarinov, V., Shapiro, Y. E., Liang, Z., Freed, J. H., and Meirovitch, E. (2002) A novel view of domain flexibility in *E. coli* adenylate kinase based on structural mode-coupling $^{15}N$ NMR relaxation, *J. Mol. Biol. 315*, 155−170.
36. Goodman, J. L., Pagel, M. D., and Stone, M. J. (2000) Relationship between protein structure and dynamics from a database of NMR-derived backbone order parameter, *J. Mol. Biol. 295*, 963−978.
37. Corpet, F. (1988) Multiple sequence alignment with hierarchical clustering, *Nucleic Acids Res. 16*, 10881−10890.
38. Dreusicke, D., Karplus, P. A., and Schulz, G. E. (1988) Refined structure of porcine cytosolic adenylate kinase at 2.1 Å resolution, *J. Mol. Biol. 199*, 359−371.
39. Berry, M. B., Meador, B., Bilderback, T., Liang, P., Glaser, M., and Phillips, G. N. (1994) The closed conformation of a highly flexible protein: the structure of *Escherichia coli* adenylate kinase with bound AMP and AMPPNP, *Proteins: Struct., Funct., Genet. 19*, 183−198.
40. Schulz, G. E., Biedermann, K., Kabsch, W., and Schirmer, R. H. (1973) Low resolution structure of adenylate kinase, *J. Mol. Biol. 80*, 857−864.
41. Knowles, J. R. (1991) To build an enzyme. *Philos. Trans. R. Soc. London, Ser. B 322*, 115−121.
42. Farnum, M. F., Magde, D., Howell, E. E., Hirai, J. T., Warren, M. S., Grimsley, J. K., and Kraut, J. (1991) Analysis of hydride transfer and cofactor fluorescence decay in mutants of dihydrofolate reductase: possible evidence for participation of enzyme molecular motions in catalysis, *Biochemistry 30*, 11567−11579.
43. Li, L., Falzone, C. J., Wright, P. E., and Benkovic, S. J. (1992) Functional role of a mobile loop of *Escherichia coli* dihydrofolate reductase in transition-state stabilization, *Biochemistry 31*, 7826−7833.
44. Williams, J. C., and McDermott, A. E. (1995) Dynamics of the flexible loop of triosephosphate isomerase: the loop motion is not ligand gated, *Biochemistry 34*, 8309−8319.
45. Burlacu-Miron, S., Perrier, V., Gilles, A.-M., Pistotnik, E., and Craescu, C. T. (1998) Structural and energetic factors of the increased thermal stability in a genetically enginnered *Escherichia coli* adenylate kinase, *J. Biol. Chem. 173*, 19102−19107.
46. Rose, T., Glaser, P., Surewicz, W. K., Mantsch, H. H., Reinstein, J., Le Blay, K., Gilles, A. M., and Barzu, O. (1991) Structural and functional consequences of amino acid substitutions in the second conserved loop of *Escherichia coli* adenylate kinase, *J. Biol. Chem. 266*, 23654−23659.
47. Okajima, T., Tanizawa, K., Yoneya, T., and Fukui, T. (1991) Role of leucine 66 in the asymmetric recognition of substrates in chicken muscle adenylate kinase, *J. Biol. Chem. 266*, 11442−11447.
48. Byeon, I.-J. L., Shi, Z., and Tsai, M.-D. (1995) Mechansim of adenylate kinase. The essential lysine helps to orient the phosphates and the active site residues to proper conformations, *Biochemistry 34*, 3172−3182.
49. Gilles, A. M., Saint Girons, I., Monnot, M., Fermandjan, S., Michelson, S., and Bârzu, O. (1986) Substitution of a serine residue for proline-87 reduces catalytic activity and increases susceptibility to proteolysis of *Escherichia coli* adenylate kinase, *Proc. Natl. Acad. Sci. U.S.A. 83*, 5798−5802.
50. Haase, G. H. W., Brune, M., Reinstein, J., Pai, E. F., Pingoud, A., and Wittinghofer, A. (1989) Adenylate kinases from thermosensitive *Escherichia coli* strains, *J. Mol. Biol. 207*, 151−162.
51. Reinstein, J., Gilles, A. M., Rose, T., Wittinghofer, A., Saint Girons, I., Bârzu, O., Surewicz, W. K., and Mantsch, H. H. (1989) Structural and catalytic role of arginine 88 in *Escherichia coli* adenylate kinase as evidenced by chemical modification and site-directed mutagenesis, *J. Biol. Chem. 264*, 8107−8112.
52. Liang, P., Phillips, G. N. J., and Glaser, M. (1991) Assignment of the nucleotide binding sites and the mechanism of substrate inhibition of *Escherichia coli* adenylate kinase, *Proteins: Struct., Funct., Genet. 9*, 28−36.
53. Kraulis, P. (1991) MOLSCRIPT: a program to produce both detailed and schematic plots of protein structures, *J. Appl. Crystallogr. 24*, 946−950.


BI0355995